Nano Research

Open Access

Research Article

Spatiotemporal quantification of nanoplastic-induced oxidative stress in 3D cortical organoids by flexible electrodes

Yiwen Jing[1,§], Xiaowen Du[2,§], Yi Zhao[1], Ting Wang[1], Yujun Zhang[1], Yanbing Yang[1], Pu Chen[3], Wanying Zhu[2]✉, Yanling Liu[1]✉, and Weihua Huang[1]✉

[1] *College of Chemistry and Molecular Sciences, Wuhan University, Wuhan 430072, China*
[2] *School of Pharmacy, Nanjing Medical University, Nanjing 211166, China*
[3] *Taikang Medical School (School of Basic Medical Sciences), Wuhan University, Wuhan 430071, China*
[§] *Yiwen Jing and Xiaowen Du contributed equally to this work.*

Cite this article: *Nano Research*, **2026**, *19*, 94908791. https://doi.org/10.26599/NR.2026.94908791

ABSTRACT: Environmental pollutant nanoplastics (NPs) cross the blood–brain barrier and induce central nervous system toxicity through multiple pathways, with oxidative stress as the core neurotoxicity initiator. However, the brain penetration depth of NPs and associated oxidative stress distribution have not yet been investigated. Herein, we developed a flexible electrochemical sensor based on platinum nanoparticle-modified carbon nanotube fiber (Pt/CNF) to minimize insertion damage. The sensor exhibits excellent mechanical compliance and high sensitivity for hydrogen peroxide (H_2O_2) detection. Using this sensor for real-time *in situ* H_2O_2 monitoring in human cortical organoids (COs), we systematically investigated the oxidative stress levels at depths of 100 and 300 μm in COs exposed to polystyrene nanoplastics (PS-NPs) for different durations within 6 days. Our results demonstrate that oxidative stress at the same depth increased with longer exposure time, and showed distinct spatial locality, concentrating primarily in the ~ 100 μm-deep penetration region. This study quantifies the spatiotemporal neurotoxicity of nanoplastics in human brain models and provides a robust technical framework for environmental health risk assessment in other tissues.

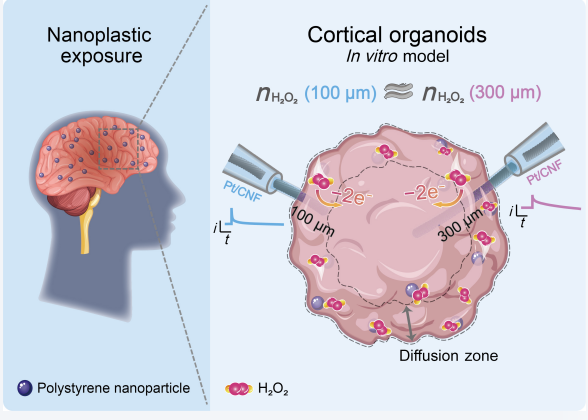

KEYWORDS: electroanalysis, flexible sensor, cortical organoids, nanoplastics, oxidative stress

1 Introduction

With the widespread application of plastic products across various fields, massive amounts of plastic waste are discharged into the natural environment, making plastic pollution one of the most pressing global environmental issues [1, 2]. Through mechanical, chemical, and biological interactions, plastic debris are degraded into microplastics (< 5 mm in diameter) and nanoplastics (< 100 nm in diameter) [3, 4]. Previous studies have shown that nanoplastics (NPs) can cross the blood–brain barrier and enter the brain, causing neurotoxicity that involves multiple biological processes [5, 6]. Oxidative stress plays a crucial role in NPs-induced nervous system damage [7, 8]. The excessive accumulation of reactive oxygen species (ROS) in the nervous system can lead to cell death and neuroinflammation [9], which is linked to neurodegenerative conditions such as Alzheimer's and Parkinson's diseases [9, 10]. Therefore, ROS quantification in the nervous system is critical for in-depth understanding the NPs-induced neurotoxicity.

Numerous animal models have revealed the potential threats of NPs to the nervous system, and studying these toxic mechanisms directly in the human brain is challenging, due to scarce resources and ethical constraints [11, 12]. To evaluate the neurotoxicity of NPs, it is important to establish an *in vitro* model that highly mimics the physiological structure and function of the human brain. Brain organoids, derived from human induced pluripotent stem cells or human embryonic stem cells, are self-assembling and three-dimensional (3D) tissue cultures that recapitulate human

Received: March 20, 2026; **Revised:** April 22, 2026
Accepted: April 29, 2026

✉Address correspondence to Wanying Zhu, wanyingzhu@njmu.edu.cn; Yanling Liu, yanlingliu@whu.edu.cn; Weihua Huang, whhuang@whu.edu.cn

brain cellular composition, architecture, and function [13–16]. Although cortical organoids (COs) do not fully recapitulate all structural and functional properties of native cortical tissue, due to current limitations in vascularization, circuit integration, and maturation [13–15], they are well-accepted *in vitro* model of cortical tissue for environmental pollutant research to assess the impacts of cadmium [17], nicotine [18], and alcohol [19] on the human brain, providing a highly promising platform for environmental toxicology. Currently, brain organoids evaluation predominantly relies on *ex vivo* or end-point detection techniques, such as immunofluorescence staining [20, 21], proteomic analysis, single-cell RNA sequencing, and quantitative polymerase chain reaction (qPCR) [22–26]. However, the oxidative stress response is a dynamically evolving process, and traditional methods fail to capture the ROS generation in 3D brain organoids over prolonged exposure. Thus, a technique capable of *in situ* quantitative tracking of dynamic ROS levels within brain organoids is essential to elucidate the neurotoxic effects of NPs.

Electrochemical sensing, as a label-free technique with fast response and excellent sensitivity, has been widely adopted for real-time monitoring of transient chemical molecules released from cells, tissues, and living organisms [27–29]. In particular, carbon nanotube-based sensors have enabled selective neurotransmitter detection with excellent robustness and anti-fouling performance, and online electrochemical monitoring of dynamic neurochemical changes and oxidative stress in neurological injury models [30–32]. Emerging flexible electrochemical sensors with remarkable mechanical compliance conform adaptively to soft biological tissues, enabling stable and precise tracking of dynamic biochemical reactions [33–37]. These devices have exhibited outstanding performance in monitoring reactive oxygen and nitrogen species (RONS) in skeletal muscle during exercise [38], neurotransmitters in the brain and gut [39–42], and various biomarkers in body fluids [43–48]. Given the distinct advantages of flexible electrochemical sensors in *in situ* monitoring and interfacing with soft biological interfaces, they hold tremendous application potential for monitoring endogenous signals within brain organoids. Nevertheless, flexible platforms for detecting internal ROS molecules within brain organoids remain unreported to date.

In this work, we developed a flexible electrochemical sensor based on platinum nanoparticle-modified carbon nanotube fibers (Pt/CNF) for *in situ* monitoring of H_2O_2 within COs exposed to polystyrene nanoparticles (PS-NPs). Helical fiber bundles were fabricated using carbon nanotubes (CNTs) as the substrate via a twisting process, followed by encapsulation in the borosilicate glass capillary and platinum electrodeposition. The as-fabricated flexible Pt/CNF electrodes were used to track the dynamic changes of H_2O_2 levels within COs after 1, 3, and 6 days of PS-NP exposure, to reveal the progress of NP-induced oxidative stress in brain tissue. Notably, by adjusting the active probing length of the electrodes, we also demonstrated the spatial distribution of oxidative stress within the 3D organoid tissues.

2 Results and discussion

2.1 Fabrication and characterization of the flexible Pt/CNF electrode

For the fabrication of flexible electrochemical sensors, CNT bundles were first twisted via a micro-motor. By tuning the dimensions of CNT bundles and twisting parameters, helical CNFs (Fig. S1 in the Electronic Supplementary Material (ESM)) with diameters ranging from 20 to 200 μm were successfully prepared. To minimize the mechanical damage to COs during the electrode implantation procedure, CNFs with a diameter of 20 μm were rationally selected as the electrode substrate. Subsequently, the CNFs were connected to lead wires and carefully inserted into glass capillaries. The SU-8 photoresist was utilized to encapsulate the connection sites and insulate the electrode body, followed by removal of the SU-8 layer at the tip via acetone etchant, yielding flexible fiber electrodes with controllable exposed lengths (Fig. S2 in the ESM). Given that the diameter of mature COs is approximately 600 μm, the exposed length of the electrode was set to 300 μm (matching the average radius of mature COs) to ensure that the electrode can detect the central region of the organoids (Fig. S3 in the ESM). To further enhance the electron transfer rate and electrochemical sensing performance of the CNF electrodes, platinum nanoparticles were electrodeposited on the CNF surface (Fig. 1(a)). Scanning electron microscopy (SEM) characterization revealed that the Pt/CNF electrode retained the helical architecture of the CNF (Fig. 1(b)). Energy-dispersive X-ray (EDX) spectroscopy mapping confirmed the dense and uniform distribution of platinum nanoparticles on the fiber surface (Fig. 1(c)).

Next, the electrochemical performance of the Pt/CNF electrodes was evaluated using 1 mM $K_3[Fe(CN)_6]$ as the redox probe. Cyclic voltammetry (CV) curves demonstrated that compared to the bare CNF, the Pt/CNF electrode exhibited a significantly larger Faradaic current, with a pair of well-defined redox peaks at 0.16 and 0.29 V (Fig. 1(d)). This indicated that the platinum nanoparticles deposited on the electrode surface could provide abundant active sites and accelerate electron transfer. The stability and reproducibility of sensors are prerequisites for reliable biological monitoring. The Pt/CNF electrode showed almost no current decay after 50 continuous CV cycles (Fig. 1(e)), indicating robust adhesion between the platinum nanoparticles and the carbon fiber, as well as the stability of the SU-8 encapsulation. Moreover, six randomly selected Pt/CNF electrodes displayed highly overlapping CV curves with nearly consistent oxidation/reduction peak currents (i_{p1}/i_{p2}) and peak potential differences (ΔE_p) (Fig. 1(f) and Fig. S4 in the ESM), confirming that the electrode preparation process has excellent repeatability and can meet the requirements of parallel experiments.

For *in situ* monitoring of oxidative stress within the COs, the electrodes must possess sufficient mechanical toughness for insertion and high tissue compliance to adapt to minute tissue deformations. When pressed against a glass substrate, the Pt/CNF electrode bent significantly without fracturing and fully recovered upon force removal (Fig. 1(g)). CV curves of the electrode in $K_3[Fe(CN)_6]$ solution were recorded before and after bending, and their results showed that the peak currents and peak potential differences remained nearly identical (Fig. 1(h) and Fig. S5 in the ESM), indicating that mechanical deformation did not degrade the sensing capabilities. The Pt/CNF electrode exhibited excellent flexibility, and SEM images showed that CNF fibers maintained structural integrity even in a knotted state (Fig. 1(i)), confirming its outstanding mechanical robustness. Furthermore, stress–strain analysis revealed Young's moduli of ~ 1.1 and 0.75 MPa for the dry and wet Pt/CNF electrodes, respectively (Fig. 1(j)). Given that the reported Young's modulus of brain organoids is ~ 2 kPa [49], the electrode is stiff enough for smooth insertion, yet soft enough to

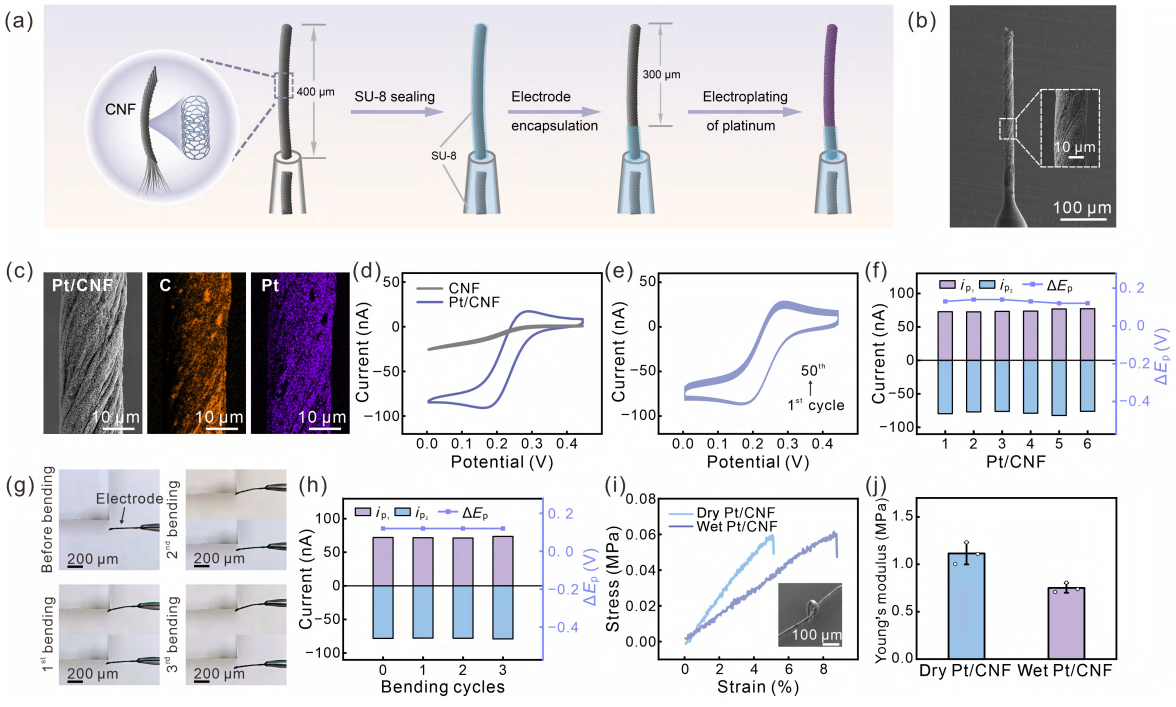

Figure 1 Design and validation of the flexible Pt/CNF electrode. (a) Schematic diagram of the Pt/CNF electrode preparation. (b) SEM image of the Pt/CNF electrode (ca. 20 μm in diameter). The inset shows a magnified view of the exposed sensing area. (c) SEM image of the Pt/CNF electrode and the corresponding EDX spectroscopy mapping images of C (orange) and Pt (purple). (d) CV curves of the bare CNF and the Pt/CNF electrodes obtained in 1 mM $K_3[Fe(CN)_6]$ solution (scan rate: 100 mV·s^{-1}). (e) Continuous CV curves (50 cycles) of the Pt/CNF electrode in 1 mM $K_3[Fe(CN)_6]$ solution. (f) Statistical plots of the peak currents and peak potential differences for six independent Pt/CNF electrodes measured in 1 mM $K_3[Fe(CN)_6]$ solution. (g) Microscopic images of the bending test performed on a Pt/CNF electrode. (h) Statistical plots of the peak currents and peak potential differences extracted from the CV curves for a Pt/CNF electrode before and after successive bending cycles. (i) Stress–strain curves of dry and wet Pt/CNF electrodes. Inset: SEM image of a knotted CNF. (j) Corresponding Young's moduli of dry and wet Pt/CNF electrodes ($n = 3$).

minimize implantation-induced mechanical damage. Collectively, these results demonstrate the successful construction of flexible microelectrodes with high electrochemical activity, stability, and tissue compliance.

2.2 Electrochemical sensing performance of Pt/CNF electrodes toward H_2O_2

To achieve quantitative detection of oxidative stress levels within COs, the electrochemical performance of the Pt/CNF electrode toward hydrogen peroxide (H_2O_2, a key indicator of oxidative stress) was first evaluated (Fig. 2(a)). CV results showed that the electrode exhibited a prominent oxidation peak at +0.6 V, which was clearly distinguishable from the background current in phosphate-buffered saline (PBS) (Fig. 2(b)), demonstrating the excellent electrocatalytic activity of the platinum nanoparticles toward H_2O_2. In addition, tests were conducted on six randomly selected Pt/CNF electrodes, and the relative standard deviation (RSD) of the limiting diffusion current at +0.6 V was only 3.14%. This highly consistent current response across different electrode batches further validates the reproducibility of our flexible sensor (Fig. S6 in the ESM). In addition, the CV responses of the 300 μm Pt/CNF electrode in 1 mM H_2O_2 remained highly consistent after 1, 2, and 3 successive bending cycles, further indicating that repeated mechanical deformation did not noticeably impair its sensing performance toward H_2O_2 (Fig. S7 in the ESM).

The detection sensitivity and linear range were subsequently evaluated using amperometry. The sensor exhibited a distinct current response to H_2O_2 concentrations as low as 100 nM (Fig. 2(c)) and maintained a good linear relationship across a wide concentration range from 100 nM to 500 μM (Fig. 2(d)). Considering the complex biochemical microenvironment within COs, the sensor's current responses to common physiological interferents, such as glutamate, ascorbic acid, and uric acid, were assessed, which were negligible compared to that of H_2O_2 (Fig. S8 in the ESM). This may be attributed to the excellent catalytic performance of Pt nanoparticles toward H_2O_2 oxidation. Altogether, these results demonstrate that the Pt/CNF sensor possesses excellent electrochemical stability and outstanding electrocatalytic performance toward the target analyte, providing a reliable tool for the quantitative monitoring of H_2O_2 within the COs.

2.3 Cortical organoid culture and nanoplastic exposure

PS-NPs derived from polystyrene products are one of the major sources of plastic pollution, and pose a severe neurotoxicity risk due to their large specific surface area, strong biofilm penetration capacity, and high cellular uptake efficiency [5, 50, 51]. As most pollutants cross the blood–brain barrier to enter brain parenchyma, we first assessed endothelial uptake and biological effects of size-varied carboxylated-PS-NPs (50, 200, and 500 nm), which were labeled with fluorescein isothiocyanate (FITC) to enable visualization of PS-NPs internalization by cells and distribution in organoid tissues. SEM, dynamic light scattering (DLS), and zeta potential characterization confirmed uniform size, good dispersibility, and stable charge of PS-NPs in cell medium (Fig. S9 in the ESM). After 24 h of incubation with endothelial cells, 50 nm PS-NPs showed the highest endothelial uptake efficiency and significantly downregulated tight junction protein ZO-1 expression

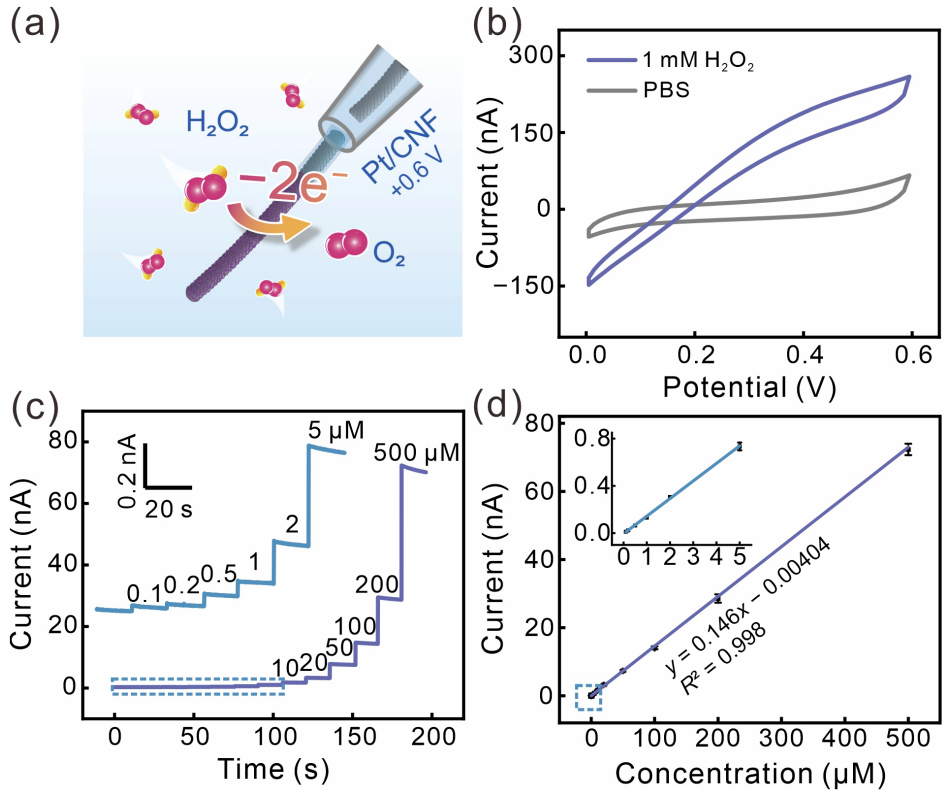

Figure 2 Electrochemical performance assessment of the Pt/CNF electrode. (a) Schematic diagram of H_2O_2 oxidation on the Pt/CNF electrode. (b) CV curves of the Pt/CNF electrode obtained in PBS and 1 mM H_2O_2 solution (scan rate: 100 mV·s^{-1}). (c) Amperometric response of the Pt/CNF electrode to increasing concentrations of H_2O_2 at a potential of +0.6 V (vs. Ag/AgCl, n = 3). The inset shows the enlargement of the amperometric response framed in blue. (d) Calibration curve of the Pt/CNF electrode for a series of increasing H_2O_2 concentrations (n = 3). The inset shows the enlargement of the calibration curve framed in blue.

(Fig. S10 in the ESM). This indicates that particles of this size are more likely to damage the integrity of the blood–brain barrier and enter the human brain, causing neurotoxicity. Consequently, 50 nm PS-NPs were selected as the model pollutant to further explore their oxidative stress effects within COs.

COs were differentiated from the human embryonic stem cell (hESC) line H9 using an established protocol [52]. Briefly, hESCs cultured in E8 medium were induced to form embryoid bodies (EBs) on day 0, and subsequently treated with SB431542 and DMH1 for 7 days to direct neural differentiation (Fig. 3(a)). Next, the EBs were transferred to a neural induction medium (NIM) and cultured up to day 40 to yield mature COs. For the nanoplastic exposure, the 40-day-old organoids were incubated in culture medium supplemented with 2 μg·mL^{-1} PS-NPs. The medium was refreshed every other day, and subsequent analyses were conducted after 1, 3, and 6 days of continuous exposure. On day 40 COs were cryosectioned and processed for immunofluorescence staining to characterize organoid development and cellular composition using cell-type-specific markers (Fig. 3(b)). FOXG1 identified forebrain regions, while PAX6 and SOX2 labeled neural progenitors of the dorsal telencephalon. Additionally, TUJ1 and DCX marked differentiating and mature neurons, and CTIP2 and TBR1 were used to target deep-layer cortical neurons. The staining results indicated robust expression of FOXG1, PAX6, and SOX2. Furthermore, dense networks of TUJ1- and DCX-positive cells were observed, along with large populations of CTIP2- and TBR1-positive cells. These results confirm the successful generation of forebrain-specific cortical organoids containing abundant neural progenitors and differentiated deep-layer cortical lineages. These results indicated that our established cortical organoids could serve as a reliable *in vitro* model of native cortical tissues.

Following the experimental protocol in Fig. 3(a), the morphological changes of the COs were monitored before and after nanoparticle exposure. By day 6, the control COs exhibited normal expansion, while PS-NP-exposed organoids showed visibly reduced overall size despite continued growth. Quantitative analysis confirmed that the cross-sectional area of the exposed group was significantly smaller than that of the control (Fig. 3(c)). To explore the underlying cellular mechanism, immunofluorescence staining was performed for the apoptotic marker caspase-3 (CAS-3) and the neuronal marker MAP2. The control group exhibited minimal CAS-3 signals and intact and dense MAP2 networks. Conversely, the PS-NP-exposed group displayed abundant CAS-3-positive cells and severely disrupted MAP2 networks (Fig. S11 in the ESM). These findings demonstrate that PS-NP exposure induces cellular apoptosis, thereby inhibiting the normal growth and tissue development of cortical organoids. To further assess the structural changes after prolonged exposure, we collected bright-field images after extending PS-NP treatment to day 8. Compared with the control group, the exposed organoids at day 8 showed marked structural collapse, including loss of compact spheroidal morphology, severe edge disruption, and abundant tissue debris (Fig. S12 in the ESM). Under these conditions, stable electrode insertion and reliable *in situ* electrochemical readout were no longer feasible. Therefore, 6 days was selected as the maximum exposure duration to preserve tissue integrity and ensure reliable neurotoxicity detection.

2.4 Depth profile and accumulation of PS-NPs in COs

To characterize the spatiotemporal distribution of PS-NPs in 3D tissues, the diffusion depth of PS-NPs within the organoids was further quantified. As shown in the confocal images (Fig. 4(a)), PS-NPs gradually crossed the outer tissue boundary over the exposure period. They penetrated the TUJ1 neural networks and migrated from the peripheral region toward the organoid core. Quantitative analysis confirmed a time-dependent penetration trend (Fig. 4(b) and Fig. S13 in the ESM). The average diffusion depth was ~ 20 μm on day 1, advanced to ~ 55 μm by day 3, and reached a maximum depth of ~ 150 μm on day 6, with over 80% of nanoparticles remaining within 100 μm of the organoid surface. These findings reveal that 50 nm PS-NPs slowly penetrate the extracellular matrix to induce cellular apoptosis, but preferentially accumulate in the peripheral region of organoids, which is consistent with the severe peripheral tissue damage observed in morphological analyses.

2.5 *In situ* quantification of H_2O_2 release within cortical organoids

Excessive generation of ROS is a key molecular indicator of nanoplastic-induced cellular damage. Therefore, *in situ* quantification of the H_2O_2 levels within COs is crucial for

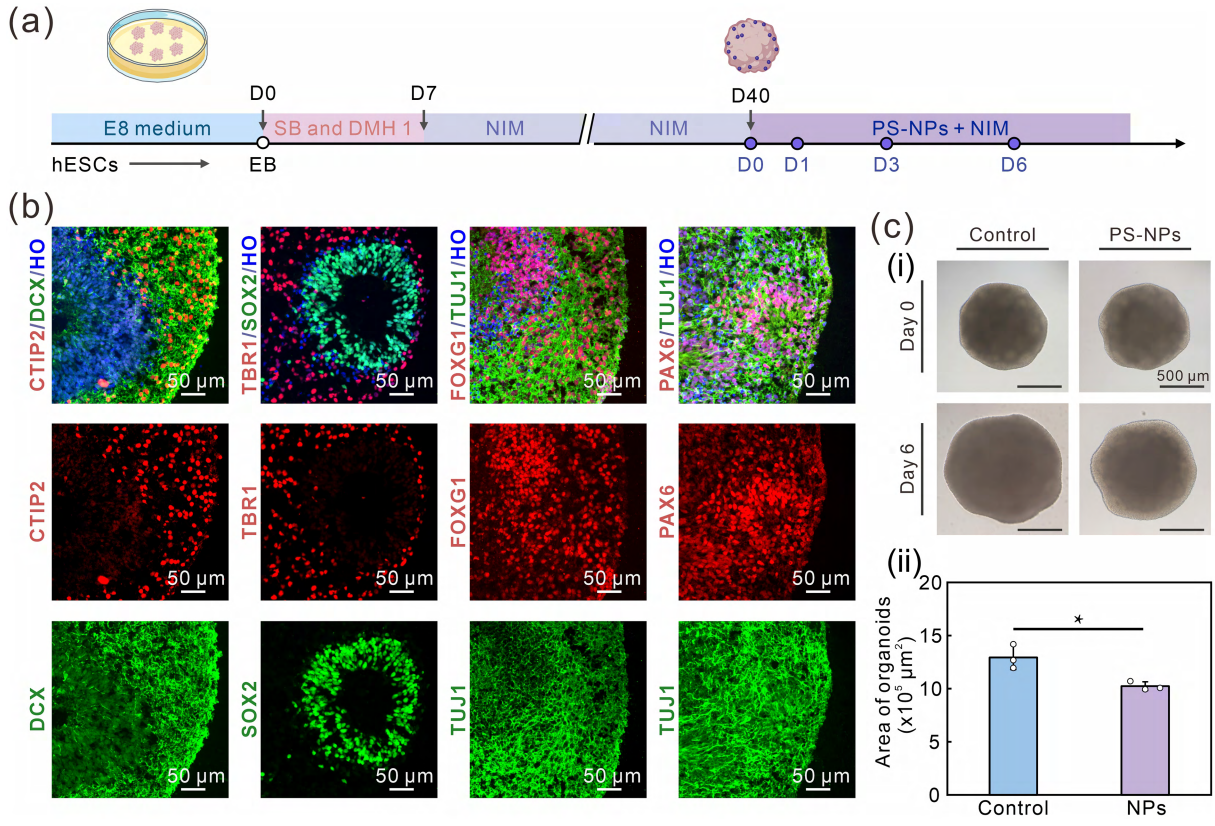

Figure 3 Differentiation of COs and PS-NPs exposure effects. (a) Schematic diagram of organoid differentiation and PS-NP exposure protocol. (b) Immunostaining for CTIP2, DCX, TBR1, SOX2, FOXG1, TUJ1, and PAX6 in cortical organoids differentiated from hESCs (H9) at day 40. (c) Representative (i) images and (ii) size quantification of organoids after PS-NPs treatment. Data are shown as the mean values ± SD ($n = 3$ and $^*P < 0.05$).

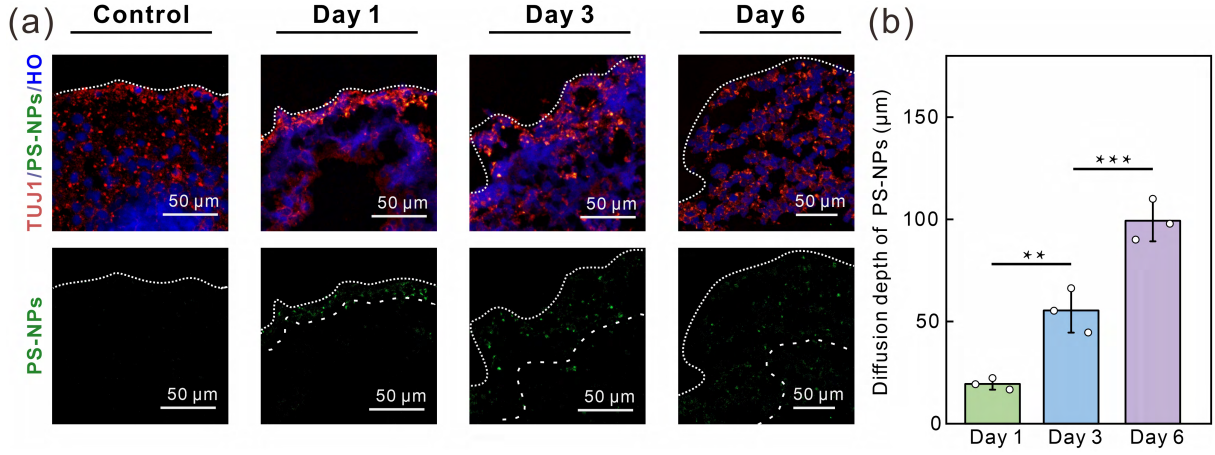

Figure 4 Penetration dynamics and accumulation of PS-NPs. (a) Confocal images of PS-NPs (green), TUJ1 (red), and nuclei (blue) in COs after 1, 3, and 6 days of PS-NP treatment. (b) Corresponding diffusion depth of PS-NPs in cortical organoids. Data are shown as the mean values ± SD ($n = 3$, $^{**}P < 0.01$, and $^{***}P < 0.001$).

understanding the neurotoxic mechanisms of nanoplastics. The electrochemical detection principle of the Pt/CNF flexible electrode used in this study is illustrated in Fig. 5(a). Benefiting from its flexibility and structural stability verified earlier, the Pt/CNF sensor could be inserted into the interior of cortical organoids and well adapted to the biological tissue microenvironment, and H_2O_2 levels are quantified based on the oxidation reaction of endogenous H_2O_2 on the electrode surface. Bright-field microscopic imaging (Fig. 5(b)) showed that the 300 μm sensing area of the electrode was fully inserted into the COs without any bending or structural failure during insertion, confirming its feasibility for *in situ* probing inside the organoids. To eliminate the interference from biological sample individual differences and ensure the reliability of the detection results, four control COs were randomly selected and multi-point parallel detection was performed on different regions of each organoid (Fig. 5(c)). The recorded endogenous H_2O_2 levels were nearly identical across different sites within the same organoid or among different organoids, with no significant differences observed. This result confirms that the established COs have excellent homogeneity at the metabolic level, providing a robust model for evaluating the neurotoxicity of nanoplastics.

Given that the penetration depth of nanoparticles in tissues increases with exposure duration (Fig. 4), it was hypothesized that the oxidative stress level inside COs would also exhibit a time-dependent trend. Therefore, the Pt/CNF electrode with a sensing length of 300 μm was employed to monitor H_2O_2 levels inside COs in both the control group and PS-NPs exposure group on day 1, 3, and 6 post-exposure. The amperometric response curves showed that immediately after electrode insertion into cortical organoids, a current rise followed by a decline was recorded in both control and experimental groups (Figs. 5(d)–5(f)). However, the current in the PS-NP-treated group showed a larger amplitude of increase and a slower decay rate, indicating a higher endogenous H_2O_2 level. The H_2O_2 content was quantified by integrating the current–time curve and converting the integral charge to the molar amount of H_2O_2 involved in the Faradaic reaction.

As shown in Fig. S14 in the ESM, the endogenous H_2O_2 level in the control group remained stable at approximately 0.1 pmol across all three time points, indicating that the standard organoid culture condition did not induce significant fluctuations in H_2O_2 levels. In contrast, H_2O_2 levels in the PS-NP-exposed group increased significantly over time, rising from ~ 0.26 pmol on day 1 to ~ 0.42 pmol on day 3, and ~ 0.60 pmol on day 6. Statistical analysis of H_2O_2 net increase (experimental minus control group) showed a steady rise from 0.16 (day 1) to 0.32 (day 3) and 0.49 pmol (day 6) (Fig. 5(g)). Collectively, these findings reveal that prolonged PS-NPs exposure and increasing penetration depth drive a continuous and cumulative intensification of oxidative stress within the COs.

2.6 Spatial distribution of nanoparticle-induced oxidative stress

Previous diffusion experiments demonstrated that PS-NPs mainly accumulated in the ~ 100 μm superficial layer of organoids by day 6 of exposure (Fig. 4). To specifically detect oxidative stress in this region, we fabricated and characterized a short Pt/CNF electrode with a 100 μm active sensing length (Fig. S15 in the ESM). As shown in the amperometric curves (Figs. 6(a)–6(c)), the 100 μm Pt/CNF electrode also recorded distinct transient current peaks upon insertion, followed by steady responses. Integration analysis revealed nearly identical H_2O_2 trends between the 100 and 300 μm electrodes. Specifically, endogenous H_2O_2 levels in the control organoids remained stable at ~ 0.035 pmol, which was roughly one-third of the value recorded by the 300 μm electrode. Whereas, the PS-NP-exposed group exhibited a significant time-dependent increase, rising from 0.19 pmol on day 1 to 0.45 pmol by day 6 (Fig. S16 in the ESM). Further comparison revealed that the total H_2O_2 detected by the 300 μm electrode was consistently higher than that of the 100 μm electrode (Fig. S16 in the ESM). This higher background signal is likely due to the extended active sensing area of the 300 μm electrode, which detects extra endogenous H_2O_2 from cells in the deeper and nanoplastic-free zones.

To eliminate background variations and accurately assess the oxidative stress induced by PS-NP internalization, the net H_2O_2 increase (experimental minus control group) recorded by 100 and 300 μm electrodes was compared (Fig. 6(d)). Statistical analysis of the 100 μm electrode data demonstrated that the PS-NPs-induced

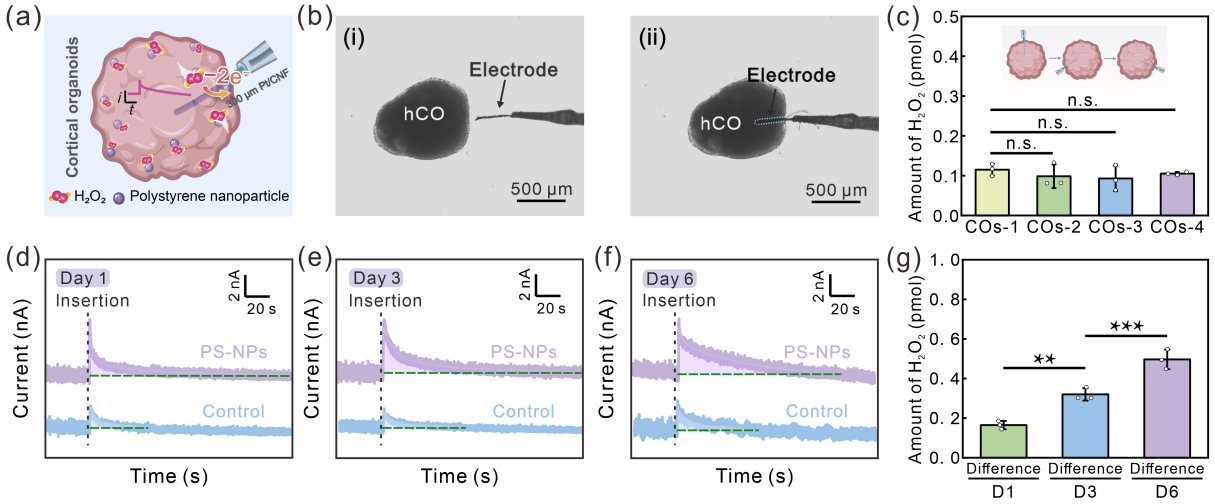

Figure 5 *In situ* monitoring of H_2O_2 release via the 300 μm Pt/CNF electrode. (a) Schematic diagrams of H_2O_2 detection in COs using a 300 μm Pt/CNF electrode. (b) Bright-field images of Pt/CNF electrode (i) before and (ii) after inserting into a CO. (c) Electrochemical detection of H_2O_2 in different regions of 4 randomly selected control COs. The inset shows schematic diagram of Pt/CNF electrode probing different regions of the COs. ((d)–(f)) Amperometric response curves of control and PS-NP-exposed groups (dashed lines: electrode insertion, baseline). (g) Net H_2O_2 increase quantification. Data are shown as the mean values ± SD (n = 3, n.s.: not significant, $^{**}P < 0.01$, and $^{***}P < 0.001$).

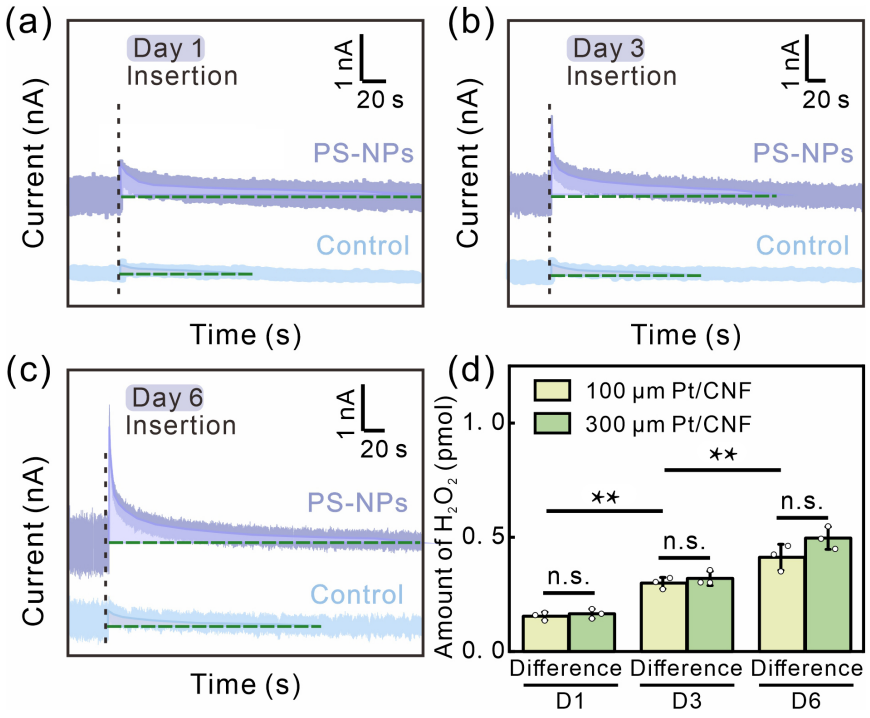

Figure 6 Spatial assessment of oxidative stress in COs using the 100 μm Pt/CNF electrode. ((a)–(c)) Amperometric response curves of control and PS-NP-exposed groups. Vertical black dashed lines indicate electrode insertion, and green dashed lines indicate integration baseline. (d) Statistical comparison of net H_2O_2 increases (experimental minus control) detected by 100 and 300 μm Pt/CNF electrodes. Data are shown as the mean values ± SD ($n = 3$ and $^{**}P < 0.01$).

H_2O_2 increment rose from 0.15 pmol on day 1 to 0.41 pmol on day 6 in a time-dependent manner. Notably, net increments from the 100 and 300 μm electrodes were nearly identical on days 1 and 3, while the 100 μm electrode recorded a slightly lower value on day 6. This minor deviation is likely attributed to a small fraction of PS-NP diffusing beyond 100 μm depth, inducing localized oxidative stress outside the shorter electrode's detection range. Altogether, the comparison of electrode signals confirms that nanoplastic-induced oxidative stress is largely confined to the nanoparticle diffusion region during the monitoring period. Deeper organoid regions unexposed to nanoparticles remain temporarily unaffected by the superficial damage, without obvious cascading amplification effect. These results demonstrate the unique advantage of our flexible Pt/CNF sensor in revealing complex spatial pathologies within 3D biological tissues.

3 Conclusions

In summary, we report a flexible electrochemical sensor based on Pt/CNF. This sensor enables *in situ* monitoring of oxidative stress within human cortical organoids to evaluate the spatiotemporal neurotoxicity of PS-NPs over a 6-day exposure period. By using electrodes with active sensing lengths of 100 and 300 μm, the spatial distribution of oxidative stress was precisely detected. The results demonstrated that nanoplastic-induced oxidative stress concentrates primarily in the ~ 100 μm-deep penetration region, without triggering cascade amplification in deeper tissues. These findings not only provide the first quantitative profile of the dynamic neurotoxicity of nanoplastics in a human 3D brain model, but also demonstrate that our depth-controllable flexible sensing strategy can serve as a robust technical framework for environmental health risk assessment and therapeutic drug screening across diverse 3D tissue model systems.

4 Experimental

4.1 Materials and instruments

Borosilicate glass capillaries (1B100-4) were purchased from World Precision Instruments (Sarasota, FL, USA). SU-8 2002 and SU-8 2015 photoresists were obtained from MicroChem Corp. (Westborough, MA, USA). Conductive carbon ink was acquired from Bare Conductive Ltd. (London, UK). Chloroplatinic acid hexahydrate ($H_2PtCl_6{\cdot}6H_2O$), 4% paraformaldehyde, and the nuclear dye Hoechst 33258 were purchased from Sigma-Aldrich (Shanghai, China). FITC-labeled carboxylated PS-NPs with diameters of 50, 200, and 500 nm were purchased from Shanghai Huizhi Biotechnology Co., Ltd. (Shanghai, China). Essential 8 medium, collagenase, PBS, Dulbecco's modified Eagle medium/F-12 nutrient mixture (Ham; DMEM/F-12), N-2 supplement, and minimum essential medium non-essential amino acids solution (MEM NEAA) were obtained from Gibco (Grand Island, NY, USA). Human umbilical vein endothelial cells (HUVECs) were provided by the Central Laboratory of Xiangya Hospital, Central South University (Changsha, China). Vitronectin, fetal bovine serum (FBS), and B-27 supplement were acquired from Thermo Fisher Scientific (Waltham, MA, USA). SB431542 was obtained from Stemgent (Cambridge, MA, USA), and DMH1 was purchased from Tocris Bioscience (Bristol, UK). Deionized (DI) water (resistivity > 18.2 MΩ·cm, Millipore Inc., USA) was used for rinsing and preparing all aqueous solutions. All other analytical-grade chemicals were obtained from Sinopharm Chemical Reagent Co., Ltd. (Shanghai, China).

SEM and EDX spectroscopy mapping images were captured using field-emission SEM (FESEM, Zeiss Sigma and Zeiss Merlin Compact, Carl Zeiss, Germany) equipped with an EDX spectrometer (X-MaxN, Oxford Instruments). Electrochemical

measurements for non-organoid experiments were performed on an electrochemical workstation (CHI 660E, CH Instruments, Shanghai, China). Young's moduli were measured using a universal testing machine equipped with a 1000 N load cell (Model 5576, INSTRON, USA). Inverted fluorescence microscopes (AxioObserver Z1 and Axiovert 200M, Zeiss) and a confocal microscope (LSM 900, Zeiss) were utilized to observe the morphological changes of cortical organoids and the internalization of PS-NPs in endothelial cells and organoids. Cortical organoid markers were imaged using a fluorescence microscope (Eclipse 80i, Nikon, Japan).

4.2 Preparation of CNFs

CNFs were prepared based on an established protocol [38]. CNT films were synthesized via chemical vapor deposition (CVD) using xylene as the carbon source, ferrocene as the catalyst, and a mixture of argon and hydrogen as the carrier gas [53]. The obtained CNT films were cut into appropriately sized strips. One end of a strip was attached to a micro-motor, while the other end was anchored to a base plate. The motor then twisted the CNT film into a helical CNF, whose diameter was determined by the initial width of the CNT film.

4.3 Fabrication of Pt/CNF electrodes

The prepared CNFs were cut into ~ 1 cm segments using a blade. Each segment was then attached to one end of a copper wire using conductive carbon ink and left to dry until the ink fully cured. This assembly was threaded through a pre-pulled glass capillary (40–50 μm in diameter). Under a microscope, the copper wire was carefully adjusted to expose approximately 400 μm of CNF from the capillary tip. The junction between the copper wire and the glass capillary was then sealed with epoxy resin (Fig. S2(a) in the ESM).

Next, the exposed CNF, along with the capillary tip, was dipped into another glass capillary containing an SU-8 mixture (SU-8 2002 and SU-8 2015 at a volume ratio of ~ 9:1) for a few seconds and swiftly withdrawn (Fig. S2(b) in the ESM, step 1), ensuring that both the CNF surface and the inner wall of the capillary were coated with SU-8. Subsequently, the SU-8-coated tip of the CNF electrode was inserted into a capillary filled with acetone to a depth of ~ 300 μm for 5 s. This dissolution step was repeated three times to completely remove the SU-8 coating from this specific region (step 2 in Fig. S2(b) in the ESM). Finally, the electrode was exposed to ultraviolet (UV) light for 30 min and baked at 70 °C for 1 h. This ensured the complete curing of the SU-8, achieving robust encapsulation and fixation of the CNF electrode.

Platinum was electrodeposited onto the CNF via cyclic voltammetry in a plating solution (10 mM H_2PtCl_6 in PBS), using the fabricated CNF as the working electrode, an Ag/AgCl reference electrode, and a Pt wire counter electrode. The potential window was set from −0.7 to 0.2 V, with an accumulated deposition charge of 1×10^{-4} C.

The 100 μm Pt/CNF electrodes were fabricated following the same protocol, except that the length of the protruding CNF was controlled at 200 μm, the acetone-etched length was adjusted to 100 μm, and the electrodeposition charge was modified to 4×10^{-5} C.

4.4 Calibration of the Pt/CNF electrode toward H_2O_2

Unless otherwise specified, all electrochemical measurements except for the cortical organoid experiments were conducted on a CHI 660E electrochemical workstation housed in a grounded Faraday cage. A standard three-electrode system was employed, with an Ag/AgCl reference electrode and a Pt wire counter electrode. A series of H_2O_2 solutions with varying concentrations were prepared by serially diluting a commercial 30% H_2O_2 stock solution. To evaluate the sensing capability of the Pt/CNF electrode, its amperometric responses to these H_2O_2 concentrations were recorded using chronoamperometry.

4.5 Cell lines and culture

The hESC line (H9, WA09, female) was maintained under feeder-free conditions in Essential 8 medium. The cells were passaged every 5–7 days onto vitronectin-coated plates using Essential 8 medium.

4.6 Generation of human cortical organoids

Human cortical organoids were generated based on an established protocol [52]. Briefly, hESCs were dissociated to form EBs and cultured in an NIM (comprising DMEM/F-12, 1% MEM NEAA, and 1% N-2 supplement) supplemented with 2 μM SB431542 and 2 μM DMH1 for neural induction. On day 7, the EBs were plated for a short period in NIM containing 10% FBS to facilitate the formation of rosette-like neuroepithelial (NE) structures. Following attachment, the cultures were maintained in serum-free basal NIM. On day 16, the NE colonies were detached and transferred to NIM supplemented with B-27 for further maturation. For the nanoplastic-treated group, PS-NPs (at a final concentration of 2 $\mu g \cdot mL^{-1}$) were added into the culture medium from day 40 onwards, and the medium was refreshed every other day.

4.7 Immunofluorescence staining of cortical organoids

Cortical organoids were fixed with 4% paraformaldehyde (PFA) for 4 h at 4 °C. The organoids were washed three times with PBS for 10 min each, and subsequently dehydrated in 20% and 30% sucrose solutions for 24 h. The dehydrated organoids were then embedded in optimal cutting temperature (O.C.T.) compound and sectioned into 10-μm-thick slices using a cryostat. The sections were washed three times with PBS and then permeabilized and blocked with 1% Triton X-100 and 5% donkey serum for 1 h at room temperature. Subsequently, the sections were incubated overnight at 4 °C with primary antibodies appropriately diluted in a solution containing 0.2% Triton X-100 and 5% donkey serum. The following day, the sections were washed three times with PBS to remove excess primary antibodies, and then incubated with secondary antibodies diluted in 5% donkey serum for 1 h at room temperature in the dark. Post-incubation, the sections were washed three times with PBS. Imaging was performed using a Nikon Eclipse 80i fluorescence microscope.

4.8 Co-staining of cells and PS-NPs

After a 24-h incubation with 10 $\mu g \cdot mL^{-1}$ FITC-PS-NPs, the cells were washed three times with PBS to remove the non-internalized nanoparticles. The cells were then fixed with 4% PFA for 7 min, followed by three PBS washes. Subsequently, the cells were permeabilized with 0.1% Triton X-100 for 7 min and washed three times with PBS. After blocking with 10% goat serum for 1 h at room temperature, the cells were incubated with an anti-ZO-1 primary antibody overnight at 4 °C. Following three additional PBS washes, the cells were incubated with a fluorophore-conjugated secondary antibody and Hoechst 33258 for 1 h. Finally, the cells were washed three times with PBS prior to fluorescence imaging.

4.9 Electrochemical detection of H_2O_2 within cortical organoids

Cortical organoids were transferred to a culture dish pre-coated with a thin layer of matrigel. A minimal amount of matrigel was then carefully applied around the base of each organoid to securely anchor it, ensuring that the upper region remained fully exposed for subsequent electrochemical probing. The dish was subsequently incubated at 37 °C for 20 min to allow complete gelation of the matrigel.

All amperometric measurements involving cortical organoids were conducted inside a well-grounded Faraday cage equipped with an inverted fluorescence microscope, a micromanipulator, and a patch-clamp amplifier. Under a 5× objective lens, the Pt/CNF electrode, connected to the headstage of the patch-clamp amplifier, was precisely positioned to the target organoid using the micromanipulator. With the assistance of the micromanipulator's vertical control knob, the active sensing region of the electrode was carefully and completely inserted into the organoid. All electrochemical recordings were performed using a two-electrode configuration, with an Ag/AgCl electrode serving as the reference/counter electrode, under a constant applied potential of +600 mV. Amperometric traces were sampled at 1 kHz and acquired using the "Pulse" software. The raw data were subsequently analyzed using the "Igor Pro" software (WaveMetrics), kindly provided by Dr. E. V. Mosharov from Columbia University.

4.10 Quantitative analysis

To convert the acquired current signals into quantitative data, the total electric charge (Q) was calculated as the area enclosed by the amperometric curve and the baseline, according to Eq. (1)

$$Q = \int i dt \tag{1}$$

where i is the current and t is the time.

The amount of electric charge produced by the oxidation of the released H_2O_2 on the electrode surface can be determined by Eq. (2)

$$Q(H_2O_2) = Q(0.6\ \mathrm{V}) \tag{2}$$

Subsequently, the corresponding charge was converted into the molar quantity of the target substance employing Faraday's law, as expressed in Eq. (3)

$$n = Q/zF \tag{3}$$

where n represents the molar amount of the redox substance, F is the Faraday constant (9.65×10^4 C·mol^{-1}) , and z is the number of transferred electron during the reaction (for H_2O_2 oxidation, $z = 2$).

4.11 Statistical analysis

All experiments were performed with at least three independent replicates, and the data are expressed as the mean ± standard deviation (SD). Statistical analyses were conducted using IBM SPSS Statistics 27 software. Statistical significance was analyzed by an independent two-sample t-test or one-way analysis of variance (ANOVA). Differences were considered statistically significant at $^*P < 0.05$, $^{**}P < 0.01$, and $^{***}P < 0.001$.

Electronic Supplementary Material: Supplementary material (details of electrode fabrication and characterization, electrochemical performance and selectivity evaluation, nanoplastic characterization and cellular uptake, immunofluorescence analysis in cortical organoids, and quantitative H_2O_2 measurements) is available in the online version of this article at https://doi.org/10.26599/NR.2026.94908791.

Data availability

All data needed to support the conclusions in the paper are presented in the manuscript and the Electronic Supplementary Material. Additional data related to this paper may be requested from the corresponding author upon request.

Acknowledgements

This work was supported by the National Key Research and Development Program of China (No. 2022YFA1104802), the National Natural Science Foundation of China (No. 22474095), and the Fundamental Research Funds for the Central Universities (No. 2042026kf0046).

Declaration of competing interest

All the contributing authors report no conflict of interests in this work.

Author contribution statement

W. H. H., Y. L. L., W. Y. Z., Y. W. J., and X. W. D. conceptualized and designed the study. Y. W. J., X. W. D., Y. Z., T. W., and Y. J. Z. performed experiments and analyzed data. Y. B. Y. supplied the carbon nanotube film. Y. W. J., X. W. D., P. C., W. Y. Z., and W. H. H. contributed to the comments and discussion on the manuscript and figures. Y. W. J., X. W. D., W. H. H., and Y. L. L. drafted and finalized the manuscript. All the authors have approved the final manuscript.

Use of AI statement

None.

References

[1] Borrelle, S. B.; Ringma, J.; Law, K. L.; Monnahan, C. C.; Lebreton, L.; McGivern, A.; Murphy, E.; Jambeck, J.; Leonard, G. H.; Hilleary, M. A. et al. Predicted growth in plastic waste exceeds efforts to mitigate plastic pollution. *Science* **2020**, *369*, 1515–1518.

[2] Bergmann, M.; Collard, F.; Fabres, J.; Gabrielsen, G. W.; Provencher, J. F.; Rochman, C. M.; van Sebille, E.; Tekman, M. B. Plastic pollution in the Arctic. *Nat. Rev. Earth Environ.* **2022**, *3*, 323–337.

[3] Vethaak, A. D.; Legler, J. Microplastics and human health. *Science* **2021**, *371*, 672–674.

[4] Gigault, J.; El Hadri, H.; Nguyen, B.; Grassl, B.; Rowenczyk, L.; Tufenkji, N.; Feng, S. Y.; Wiesner, M. Nanoplastics are neither microplastics nor engineered nanoparticles. *Nat. Nanotechnol.* **2021**, *16*, 501–507.

[5] Ma, Y.; Yang, H. T.; Niu, S. Y.; Guo, M. H.; Xue, Y. Y. Mechanisms of micro- and nanoplastics on blood–brain barrier crossing and neurotoxicity: Current evidence and future perspectives. *Neurotoxicology* **2025**, *109*, 92–107.

[6] Cho, Y.; Seo, E. U.; Hwang, K. S.; Kim, H.; Choi, J.; Kim, H. N. Evaluation of size-dependent uptake, transport and cytotoxicity of polystyrene microplastic in a blood–brain barrier (BBB) model. *Nano Converg.* **2024**, *11*, 40.

[7] Zhang, X. X.; Zhang, X. X.; Ma, L. P. New Horizons in

micro/nanoplastic-induced oxidative stress: Overlooked free radical contributions and microbial metabolic dysregulations in anaerobic digestion. *Environ. Sci. Technol.* **2024**, *58*, 21251–21264.

[8] Prüst, M.; Meijer, J.; Westerink, R. H. S. The plastic brain: Neurotoxicity of micro- and nanoplastics. *Part. Fibre Toxicol.* **2020**, *17*, 24.

[9] Tönnies, E.; Trushina, E. Oxidative stress, synaptic dysfunction, and Alzheimer's disease. *J. Alzheimers Dis.* **2017**, *57*, 1105–1121.

[10] Radi, E.; Formichi, P.; Battisti, C.; Federico, A. Apoptosis and oxidative stress in neurodegenerative diseases. *J. Alzheimers Dis.* **2014**, *42 Suppl 3*, S125–S152.

[11] Hartung, T. Toxicology for the twenty-first century. *Nature* **2009**, *460*, 208–212.

[12] Hodge, R. D.; Bakken, T. E.; Miller, J. A.; Smith, K. A.; Barkan, E. R.; Graybuck, L. T.; Close, J. L.; Long, B.; Johansen, N.; Penn, O. et al. Conserved cell types with divergent features in human versus mouse cortex. *Nature* **2019**, *573*, 61–68.

[13] Amiri, A.; Coppola, G.; Scuderi, S.; Wu, F. N.; Roychowdhury, T.; Liu, F. C.; Pochareddy, S.; Shin, Y.; Safi, A.; Song, L. Y. et al. Transcriptome and epigenome landscape of human cortical development modeled in organoids. *Science* **2018**, *362*, eaat6720.

[14] Uzquiano, A.; Kedaigle, A. J.; Pigoni, M.; Paulsen, B.; Adiconis, X.; Kim, K.; Faits, T.; Nagaraja, S.; Antón-Bolaños, N.; Gerhardinger, C. et al. Proper acquisition of cell class identity in organoids allows definition of fate specification programs of the human cerebral cortex. *Cell* **2022**, *185*, 3770–3788.e27.

[15] He, Z. S.; Dony, L.; Fleck, J. S.; Szałata, A.; Li, K. X.; Slišković, I.; Lin, H. C.; Santel, M.; Atamian, A.; Quadrato, G. et al. An integrated transcriptomic cell atlas of human neural organoids. *Nature* **2024**, *635*, 690–698.

[16] Li, Y.; Zeng, P. M.; Wu, J.; Luo, Z. G. Advances and applications of brain organoids. *Neurosci. Bull.* **2023**, *39*, 1703–1716.

[17] Huang, Y.; Guo, X. H.; Lu, S. Y.; Chen, Q. Q.; Wang, Z. Q.; Lai, L.; Liu, Q.; Zhu, X. Z.; Luo, L.; Li, J. Y. et al. Long-term exposure to cadmium disrupts neurodevelopment in mature cerebral organoids. *Sci. Total Environ.* **2024**, *912*, 168923.

[18] Wang, Y. Q.; Wang, L.; Zhu, Y. J.; Qin, J. H. Human brain organoid-on-a-chip to model prenatal nicotine exposure. *Lab Chip* **2018**, *18*, 851–860.

[19] Adams, J. W.; Negraes, P. D.; Truong, J.; Tran, T.; Szeto, R. A.; Guerra, B. S.; Herai, R. H.; Teodorof-Diedrich, C.; Spector, S. A.; Del Campo, M. et al. Impact of alcohol exposure on neural development and network formation in human cortical organoids. *Mol. Psychiatry* **2023**, *28*, 1571–1584.

[20] Shan, S.; Zhang, Y. F.; Zhao, H. W.; Zeng, T.; Zhao, X. L. Polystyrene nanoplastics penetrate across the blood–brain barrier and induce activation of microglia in the brain of mice. *Chemosphere* **2022**, *298*, 134261.

[21] Tao, M. D.; Wang, C.; Zheng, Z. L.; Gao, W. W.; Chen, Q.; Xu, M.; Zhu, W. Y.; Xu, L.; Han, X.; Guo, X. et al. Nanoplastics exposure-induced mitochondrial dysfunction contributes to disrupted stem cell differentiation in human cerebral organoids. *Ecotoxicol. Environ. Saf.* **2024**, *285*, 117063.

[22] Park, D. S.; Kozaki, T.; Tiwari, S. K.; Moreira, M.; Khalilnezhad, A.; Torta, F.; Olivié, N.; Thiam, C. H.; Liani, O.; Silvin, A. et al. iPS-cell-derived microglia promote brain organoid maturation via cholesterol transfer. *Nature* **2023**, *623*, 397–405.

[23] Bagley, J. A.; Reumann, D.; Bian, S.; Lévi-Strauss, J.; Knoblich, J. A. Fused cerebral organoids model interactions between brain regions. *Nat. Methods* **2017**, *14*, 743–751.

[24] Antón-Bolañnos, N.; Faravelli, I.; Faits, T.; Andreadis, S.; Kastli, R.; Trattaro, S.; Adiconis, X.; Wei, A. Q.; Sampath Kumar, A.; Di Bella, D. J. et al. Brain chimeroids reveal individual susceptibility to neurotoxic triggers. *Nature* **2024**, *631*, 142–149.

[25] Du, Z. L.; Zang, Z. L.; Luo, J.; Liu, T. Y.; Yang, L.; Cai, Y.; Wang, L. Y. W.; Zhang, D. D.; Zhao, J. H.; Gao, J. W. et al. Chronic exposure to (*2R, 6R*)-hydroxynorketamine induces developmental neurotoxicity in hESC-derived cerebral organoids. *J. Hazard. Mater.* **2023**, *453*, 131379.

[26] Abdulla, A.; Yan, H. N.; Chen, S. J.; Wu, L. Q.; Chen, X. S.; Zhang, Y. Z.; Zhang, M. L.; Zhuang, T. Y.; Ahmad, K. Z.; Lin, J. J. et al. A multichannel microfluidic device for revealing the neurotoxic effects of bisphenol S on cerebral organoids under low-dose constant exposure. *Biosens. Bioelectron.* **2025**, *267*, 116754.

[27] Phan, N. T. N.; Li, X. C.; Ewing, A. G. Measuring synaptic vesicles using cellular electrochemistry and nanoscale molecular imaging. *Nat. Rev. Chem.* **2017**, *1*, 0048.

[28] Yang, T.; Shen, T. J.; Duan, B. Y.; Liu, Z. Y.; Wang, C. X. *In vivo* electrochemical biosensing technologies for neurochemicals: Recent advances in electrochemical sensors and devices. *ACS Sens.* **2025**, *10*, 100–121.

[29] Wu, F.; Yu, P.; Mao, L. Q. Multi-spatiotemporal probing of neurochemical events by advanced electrochemical sensing methods. *Angew. Chem., Int. Ed.* **2023**, *62*, e202208872.

[30] Xiang, L.; Lin, Y. Q.; Yu, P.; Su, L.; Mao, L. Q. Laccase-catalyzed oxidation and intramolecular cyclization of dopamine: A new method for selective determination of dopamine with laccase/carbon nanotube-based electrochemical biosensors. *Electrochim. Acta* **2007**, *52*, 4144–4152.

[31] Harreither, W.; Trouillon, R.; Poulin, P.; Neri, W.; Ewing, A. G.; Safina, G. Carbon nanotube fiber microelectrodes show a higher resistance to dopamine fouling. *Anal. Chem.* **2013**, *85*, 7447–7453.

[32] Liu, K.; Yu, P.; Lin, Y. Q.; Wang, Y. X.; Ohsaka, T.; Mao, L. Q. Online electrochemical monitoring of dynamic change of hippocampal ascorbate: Toward a platform for *in vivo* evaluation of antioxidant neuroprotective efficiency against cerebral ischemia injury. *Anal. Chem.* **2013**, *85*, 9947–9954.

[33] Zhao, Y.; Jin, K. Q.; Li, J. D.; Sheng, K. K.; Huang, W. H.; Liu, Y. L. Flexible and stretchable electrochemical sensors for biological monitoring. *Adv. Mater.* **2025**, *37*, 2305917.

[34] Liu, Y. L.; Huang, W. H. Stretchable electrochemical sensors for cell and tissue detection. *Angew. Chem., Int. Ed.* **2021**, *60*, 2757–2767.

[35] Fan, W. T.; Huang, W. H.; Liu, Y. L. Stretchable electrochemical sensors: From electrode fabrication to cell mechanotransduction monitoring. *Chin. J. Chem.* **2023**, *41*, 443–457.

[36] Yan, J.; Qin, Y.; Fan, W. T.; Wu, W. T.; Lv, S. W.; Yan, L. P.; Liu, Y. L.; Huang, W. H. Plasticizer and catalyst co-functionalized PEDOT:PSS enables stretchable electrochemical sensing of living cells. *Chem. Sci.* **2021**, *12*, 14432–14440.

[37] Zhao, Y.; Fan, W. T.; Jin, K. Q.; Yan, J.; Qi, Y. T.; Huang, W. H.; Liu, Y. L. Real-time quantification of nanoplastics-induced oxidative stress in stretching alveolar cells. *ACS Nano* **2024**, *18*, 6176–6185.

[38] Li, J. X.; Fan, W. T.; Sun, M. Y.; Zhao, Y.; Lu, Y. F.; Yang, Y. B.; Huang, W. H.; Liu, Y. L. Flexible fiber sensors for real-time monitoring of redox signaling molecules in exercise-mimicking engineered skeletal muscle. *Angew. Chem., Int. Ed.* **2025**, *64*, e202421684.

[39] Li, J. X.; Liu, Y. X.; Yuan, L.; Zhang, B. B.; Bishop, E. S.; Wang, K. C.; Tang, J.; Zheng, Y. Q.; Xu, W. H.; Niu, S. M. et al. A tissue-like neurotransmitter sensor for the brain and gut. *Nature* **2022**, *606*, 94–101.

[40] Liu, Y. L.; Chen, Y.; Fan, W. T.; Cao, P.; Yan, J.; Zhao, X. Z.; Dong, W. G.; Huang, W. H. Mechanical distension induces serotonin release from intestine as revealed by stretchable electrochemical sensing. *Angew. Chem., Int. Ed.* **2020**, *59*, 4075–4081.

[41] Hong, F.; Zhu, X. Y.; Fan, W. T.; Li, J. D.; Lu, Y. F.; Mao, L. B.; Huang, W. H.; Liu, Y. L. Stretchable sensor-integrated microfluidic chip for monitoring fatty acid-enhanced serotonin release from the intestinal epithelium. *Anal. Chem.* **2025**, *97*, 20484–20492.

[42] Feng, J. Y.; Fang, Y.; Wang, C.; Chen, C. R.; Tang, C. Q.; Guo, Y.;

Wang, L. Y.; Yang, Y. Q.; Zhang, K. L.; Wang, J. J. et al. All-polymer fiber organic electrochemical transistor for chronic chemical detection in the brain. *Adv. Funct. Mater.* **2023**, *33*, 2214945.

[43] Li, J. M.; Liu, J. Y.; Wu, Z. Y.; Shang, X.; Li, Y.; Huo, W. X.; Huang, X. Fully printed and self-compensated bioresorbable electrochemical devices based on galvanic coupling for continuous glucose monitoring. *Sci. Adv.* **2023**, *9*, eadi3839.

[44] Wang, L. Y.; Xie, S. L.; Wang, Z. Y.; Liu, F.; Yang, Y. F.; Tang, C. Q.; Wu, X. Y.; Liu, P.; Li, Y. J.; Saiyin, H. et al. Functionalized helical fibre bundles of carbon nanotubes as electrochemical sensors for long-term *in vivo* monitoring of multiple disease biomarkers. *Nat. Biomed. Eng.* **2020**, *4*, 159–171.

[45] Zou, K. Y.; Li, Q. M.; Li, D.; Jiao, Y. D.; Wang, L.; Li, L. H.; Wang, J. C.; Li, Y. R.; Gao, R.; Li, F. Y. et al. A highly selective implantable electrochemical fiber sensor for real-time monitoring of blood homovanillic acid. *ACS Nano* **2024**, *18*, 7485–7495.

[46] Li, R. F.; Qi, H.; Ma, Y.; Deng, Y. P.; Liu, S. N.; Jie, Y. S.; Jing, J. Z.; He, J. L.; Zhang, X.; Wheatley, L. et al. A flexible and physically transient electrochemical sensor for real-time wireless nitric oxide monitoring. *Nat. Commun.* **2020**, *11*, 3207.

[47] Deng, Y. P.; Qi, H.; Ma, Y.; Liu, S. B.; Zhao, M. Y.; Guo, Z. H.; Jie, Y. S.; Zheng, R.; Jing, J. Z.; Chen, K. T. et al. A flexible and highly sensitive organic electrochemical transistor-based biosensor for continuous and wireless nitric oxide detection. *Proc. Natl. Acad. Sci. USA* **2022**, *119*, e2208060119.

[48] Li, Q. M.; Li, D.; Lu, J.; Zou, K. Y.; Wang, L.; Jiao, Y. D.; Wang, M. S.; Gao, R.; Song, J.; Li, Y. R. et al. Interface-stabilized fiber sensor for real-time monitoring of amniotic fluid during pregnancy. *Adv. Mater.* **2024**, *36*, 2307726.

[49] Ryu, H.; Park, Y.; Luan, H. W.; Dalgin, G.; Jeffris, K.; Yoon, H. J.; Chung, T. S.; Kim, J. U.; Kwak, S. S.; Lee, G. et al. Transparent, compliant 3D mesostructures for precise evaluation of mechanical characteristics of organoids. *Adv. Mater.* **2021**, *33*, 2100026.

[50] Kopatz, V.; Wen, K.; Kovács, T.; Keimowitz, A. S.; Pichler, V.; Widder, J.; Vethaak, A. D.; Hollóczki, O.; Kenner, L. Micro- and nanoplastics breach the blood–brain barrier (BBB): Biomolecular corona's role revealed. *Nanomaterials* **2023**, *13*, 1404.

[51] Vojnits, K.; de León, A.; Rathore, H.; Liao, S.; Zhao, M.; Gibon, J.; Pakpour, S. ROS-dependent degeneration of human neurons induced by environmentally relevant levels of micro- and nanoplastics of diverse shapes and forms. *J. Hazard. Mater.* **2024**, *469*, 134017.

[52] Xu, L.; Ding, H. B.; Wu, S. S.; Xiong, N. K.; Hong, Y.; Zhu, W. Y.; Chen, X. Y.; Han, X.; Tao, M. D.; Wang, Y. H. et al. Artificial meshed vessel-induced dimensional breaking growth of human brain organoids and multiregional assembloids. *ACS Nano* **2024**, *18*, 26201–26214.

[53] Yang, Y. B.; Yang, X. D.; Liang, L.; Gao, Y. Y.; Cheng, H. Y.; Li, X. M.; Zou, M. C.; Ma, R. Z.; Yuan, Q.; Duan, X. F. Large-area graphene-nanomesh/carbon-nanotube hybrid membranes for ionic and molecular nanofiltration. *Science* **2019**, *364*, 1057–1062.